


## Numerical study and sensitivity analysis of heat transfer characteristics of heat exchangers in a high-power free-piston Stirling generator

Haitao Wang<sup>a,b</sup>, Yanyan Chen<sup>b,\*</sup>, Shunmin Zhu<sup>c,\*</sup> , Limin Zhang<sup>b</sup>, Guoyao Yu<sup>b</sup>,  
Huifang Kang<sup>a</sup>, Ercang Luo<sup>b,d</sup>

<sup>a</sup> School of Mechanical Engineering, Beijing Institute of Technology, Beijing 100081, China

<sup>b</sup> Key Laboratory of Cryogenic Science and Technology, Technical Institute of Physics and Chemistry, Chinese Academy of Sciences, Beijing 100190, China

<sup>c</sup> Department of Engineering, Durham University, Durham DH1 3LE, UK

<sup>d</sup> University of Chinese Academy Sciences, Beijing 100049, China

### ARTICLE INFO

#### Keywords:

Free-piston  
Stirling engine  
Oscillating flow  
Heat transfer characteristics  
Heat exchanger

### ABSTRACT

The increasing of deep space exploration missions has promoted research on space nuclear power systems worldwide. Stirling generators, especially free-piston Stirling generators (FPSGs), are a promising dynamic energy conversion technology for space nuclear power systems. As core components of a Stirling system, oscillating flow heat exchangers (OFHXs) have a crucial impact on the performance of the system. Unfortunately, a comprehensive comparison between low-order numerical models and the computational fluid dynamics (CFD) simulations on the engine core unit (ECU) is lacking. Meanwhile, the heat transfer characteristics of the ECU at high power levels remain poorly understood. Therefore, in this paper, a 10 kW FPSG is taken as an example, and its ECU is numerically simulated using Sage software and CFD simulation, respectively. Then the results of the two different numerical methods are compared under rated conditions, and we concluded the Sage model can effectively characterize the heat transfer distributions within the ECU. Furthermore, the heat transfer characteristics of the ECU were analysed in detail using the Sage model. The results indicate that a 90° change in the acoustic phase difference of the ECU could lead to a 32 kW variation in acoustic power of the high-temperature heat exchanger (HHX), and the regenerator transitions from amplifying acoustic power to beginning to consume acoustic power. This demonstrates that the heat transfer characteristics of the OFHX are sensitive to the distribution of the acoustic phase difference. This work contributes to the development of the ECU for high-power FPSGs, which will strengthen the foundation for their subsequent integration with micro nuclear reactors.

### Introduction

With the increasing of deep space exploration missions, space nuclear power systems will be a more suitable solution to these missions compared with solar and chemistry batteries, due to their advantage of being independent of solar flux, strong environmental adaptability, and easy to be scaled up [1,2]. A crucial element of a space nuclear power system is the energy converter. According to the involvement of mechanical moving components in the energy conversion process, energy converters can be categorized into two types, namely static and dynamic converters [3]. As a highly efficient dynamic converter, the free-piston Stirling generator (FPSG) has drawn much attention around the world for the power range between 0.1–100 kW, including the US [4], the EU [5], Japan [6], China [7], and South Korea [8]. The prominent

advantages of FPSGs lie in, on the one hand, their simple structure with few moving parts, and on the other hand, their compatibility with diverse energy sources [9]. The former enables them to have high reliability and low maintenance costs, while the latter allows them to harness different clean energy sources such as nuclear, solar, biomass, and geothermal energy [10].

FPSGs generally contain a free-piston Stirling engine (FPSE) and a linear alternator (LA). The FPSE and the thermoacoustic engine (TAE) both utilize thermodynamic principles to convert thermal energy into mechanical work, but they are achieved through different mechanisms. FPSE uses a sealed cylinder with a freely solid moving piston (in some cases using a liquid piston), allowing the working fluid to expand and compress when absorbing and releasing heat, while TAE relies on sound waves generated by temperature gradients to produce oscillating pressure changes [11,12]. The core components of FPSE, particularly high-

\* Corresponding authors.

E-mail addresses: [yychen@mail.ipc.ac.cn](mailto:yychen@mail.ipc.ac.cn) (Y. Chen), [shunmin.zhu@durham.ac.uk](mailto:shunmin.zhu@durham.ac.uk) (S. Zhu).

Nomenclature			
<i>Abbreviations</i>		$c$	Prandtl number
AHX	Ambient-temperature heat exchanger	$q_w$	Surface heat flux of wall, W/m <sup>2</sup>
CFD	Computational fluid dynamics	$Q$	Wall heat flux, W
ECU	Engine core unit	$Re$	Reynolds number
FPSE	Free-piston Stirling engine	$S_x$	Wetted perimeter, m <sup>2</sup>
FPSE	Free-piston Stirling generator	$T$	Average gas temperature, K
HHX	High-temperature heat exchanger	$T_f$	Velocity weighted average temperature, K
LA	Linear alternator	$T_w$	Wall temperature, K
OFHX	Oscillating flow heat exchanger	$u$	Gas velocity, m/s
REG	Regenerator	$U$	Volume flow rate, m <sup>3</sup> /s
<i>Symbols</i>		$\vec{V}$	Gas velocity, m/s
$A$	Cross-sectional area, m <sup>2</sup>	$W_a$	Time-average acoustic power, W
$c_p$	Specific heat of gas, J/(kg·K)	$X_p$	Displacement of the power piston, mm
$C_f$	Inertial resistance coefficient, m <sup>-1</sup>	$x$	Axial length, mm
$d_h$	Hydraulic diameter, mm	$\alpha$	Porosity
$e$	Specific total gas energy	$\varepsilon$	Average height of irregular surfaces, m
$F$	Represents the viscous pressure gradient	$\theta_{p,U}$	Phase difference between p and U, degree, °
$f$	Resistance coefficient	$\mu$	Dynamic viscosity, Pa·s
$K$	Permeability, m	$\rho$	Density, kg/cm <sup>3</sup>
$K_{loss}$	Total local loss coefficient	$\phi$	Dissipation function
$k$	Thermal conductivity, W/(m·K)	<i>Subscripts</i>	
$L$	Length of heat exchanger, m	1	First-order
$\dot{m}$	Mass flow rate, kg/s	comp	Compression space
$Nu$	Nusselt number	exp1	Expansion space 1
$p$	Pressure wave, Pa	in	Inlet
		out	Outlet

temperature heat exchangers (HHX), regenerators (REG), and ambient-temperature heat exchangers (AHX), play a crucial role in determining flow and heat transfer performance as well as the output performance of the engine. However, these oscillating flow heat exchangers (OFHXs) exhibit distinct heat transfer characteristics compared to unidirectional flow heat exchangers [13]. The reciprocating and oscillating flow of the working fluid and the complexity of the heat exchangers' geometric structure make traditional design methods for unidirectional flow heat exchangers inapplicable to the heat exchangers of FPSE [14,15]. Therefore, efforts should be made to fully understand the working mechanisms of OFHXs while providing quantitative descriptions in designing and optimizing these heat exchangers.

Generally speaking, research methods for OFHXs can be divided into three types, namely theoretical calculations, numerical analysis, and experimental studies. In theoretical fluid flow and heat transfer calculations, linear or weakly nonlinear thermoacoustic theory is used mostly. It provides good explanations for linear and weakly nonlinear thermoacoustic phenomena. Still, it cannot provide precise results for understanding the multi-physics coupling and strong nonlinear situations that arise at high frequencies and speeds. Richardson and Tyler [16] proposed the time-averaged steady-flow equivalent model, which utilizes time-averaged values within half of an acoustic period to handle the gas parameters in oscillating flows. Gedeon [17] presented a characterization method for the space-cycle averaged Nusselt number and demonstrated that relevant parameters can be applied to the energy and momentum equations. This approach eliminates the need for precise phase difference measurements between heating temperature and heat flux. Nika et al. [18] studied a method for characterizing the Nusselt number and derived first-order formulas for friction and heat transfer coefficients in microchannel heat exchangers under oscillating flow conditions; their study revealed that heat transfer attributes in microchannel heat exchangers under oscillating flow are impacted by the time characteristic and dynamic features of heat conversion efficiency. Liu and Garrett [19] proposed the use of complex Nusselt numbers to

describe heat transfer in oscillating flow induced by compression and expansion effects; they concluded that precise heat transfer characterization in porous media can be obtained without the need for temperature measurements or auxiliary heat exchangers, through the combination of the thermal viscous function and Nusselt number.

Numerical computation describes physical processes by developing appropriate numerical models. These models are primarily categorized into low-order numerical models and higher-order or computational fluid dynamics (CFD) models.

Low-order numerical models are simplified mathematical models that describe the variation and interaction of key parameters such as heat transfer, acoustic-pressure vibration, and fluid dynamics through a series of equations. These models feature low computational cost and fast computational speed, hence can provide an overall characterization of flow and heat transfer. However, due to their simplification of details, these models are only suitable for qualitative analysis and preliminary prediction of heat transfer phenomena in thermoacoustic oscillating flows, rather than providing accurate quantitative results. Such as, Swift et al. [20] created software for designing low-amplitude thermoacoustic systems. Utilizing a model of boundary layer conduction, the software calculates the coefficient for heat transfer. This coefficient is defined as the ratio of the minimum value between the hydraulic radius of the gas channel inside the heat exchanger and the depth of thermal penetration.

Different from low-order numerical models, CFD simulations focus on capturing the nonlinear phenomena present in physical structures. Currently, the used CFD models can be broadly categorized into two main groups: the first category is single engine core and the other category is based on full Stirling systems. These approaches further distinguish between models that deal with microscale resolution and those that involve macroscopic porous media methods to simulate engine cores. The former involves detailed geometric modelling of the computational domain using "high-fidelity models" to capture the characteristics of three-dimensional structures, including the associated calculation of the REG [21,22]. The latter simulates a complete Stirling

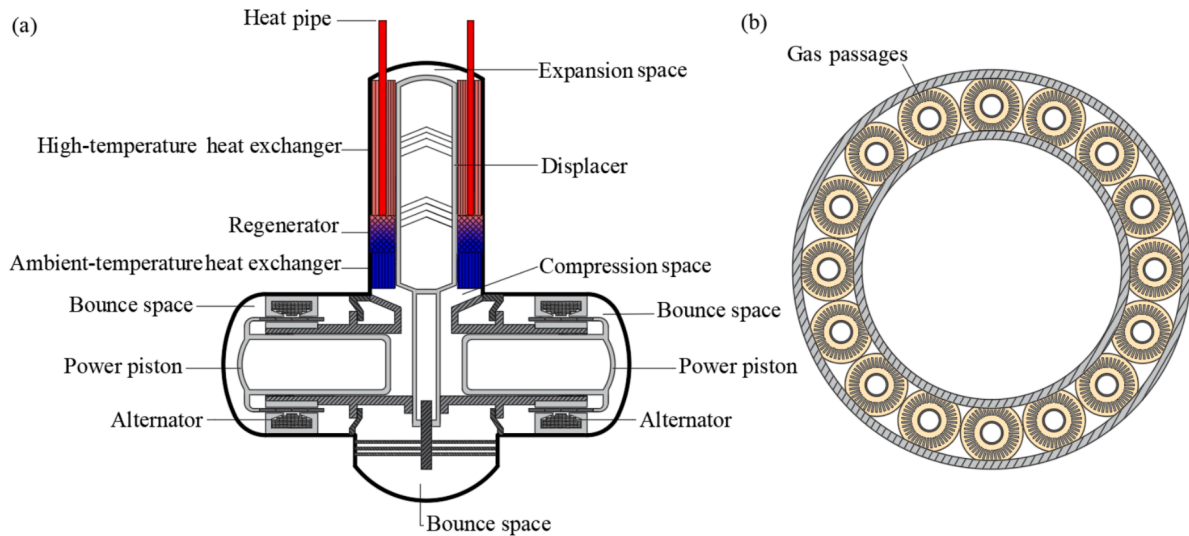


Fig. 1. (a) Schematic of the FPSG that is capable of integrating heat pipes and (b) cross-section view along the radial direction of the HHX.

Table 1  
Structural parameters of the FPSG.

Structural parameters	Values
Length of HHX	250 mm
Gap width of HHX's fins	1.3 mm
Gap height of HHX's fins	10 mm
Outer diameter of REG	248 mm
Inner diameter of REG	150 mm
Length of REG	52 mm
Porosity of REG	89.7 %
Length of AHX	70 mm
Inner diameter of the AHX's tube	2 mm

Table 2  
Operating conditions of the FPSG.

Operating conditions	Values
Working gas	helium
Working frequency	50 Hz
Mean pressure	9 MPa
Temperature of HHX	823 K
Temperature of AHX	333 K
Thermoacoustic efficiency	40.64 %
Output electrical power	10.77 kW

Table 3  
Parameters of the same section for the two models.

Variable	Sage model	CFD model	Deviations
$\dot{m}_{1, comp}$ (kg/s)	0.6346@0°	0.6308@0°	0.6 %
$\dot{m}_{1, exp1}$ (kg/s)	0.3116@-43.05°	0.3223@-40.21°	3.4 %
$p_{1, comp}$ (Pa)	884607.2@0°	908421@0°	2.7 %
$p_{1, exp1}$ (Pa)	844263.3@-3.74°	762732@-7.84°	9.6 %
$W_{a, AHX,out}$ (W)	12,677	13,805	8.9 %
$W_{a, HHX,in}$ (W)	23622.67	22,106	6.4 %
$Q_{AHX}$ (W)	-12700	-12140	4.4 %
$Q_{HHX}$ (W)	23,650	20,293	14.2 %

engine system [23]. In this context, the REG, as a component of the engine core unit (ECU), is typically represented as a porous media model to facilitate the study of the system's overall performance. Bitsikas et al. [24] segmented the REG of a  $\beta$  Stirling engine into multiple sections for analysis on flow and heat transfer dynamics by CFD. The REG was partitioned into three regions based on temperature profiles. In the initial and final 20 % of its length, temperature variations were

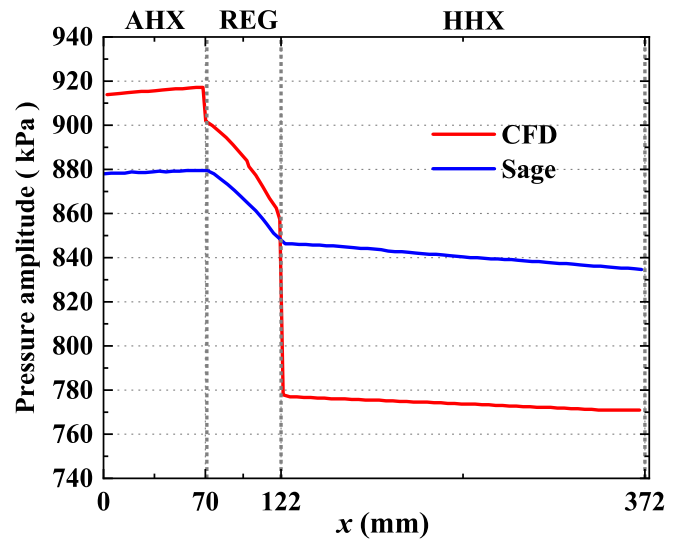


Fig. 2. Comparison of pressure amplitude distributions in the ECU under the rated conditions obtained by the two different numerical methods.

represented using a 2 nd-order polynomial equation. Across the central 60 % of the REG, there was a linear relationship between temperature and length. By deriving equations to capture heat transfer and temperature variations over space and time, accurate predictions for both fluid and metal matrix properties were achieved at specific lengths and time points. El-Ghafour et al. [25] also devised a three-dimensional CFD model to study the ECU of an FPSE. They focused on flow and heat transfer distribution in the engine cycle, assessing the accuracy of various eddy-viscosity models. Notably, the corrected  $k-\epsilon$  turbulence model demonstrated an average deviation of approximately 4 % when compared with experimental data, indicating its reliability and efficacy in predicting heat transfer dynamics within the engine system.

In experimental studies, the oscillating fluid's flow and temperature fields are mainly assessed through the use of thermocouples, infrared thermography, and other devices. However, due to the limited laboratory conditions, obtaining accurate data for the flow field and temperature field is costly. Additionally, the achievable experimental test conditions are often difficult to completely cover the all operating conditions of the system that need to be considered. As a result, most experiments on OFHXs focus solely on experimental tests of the single

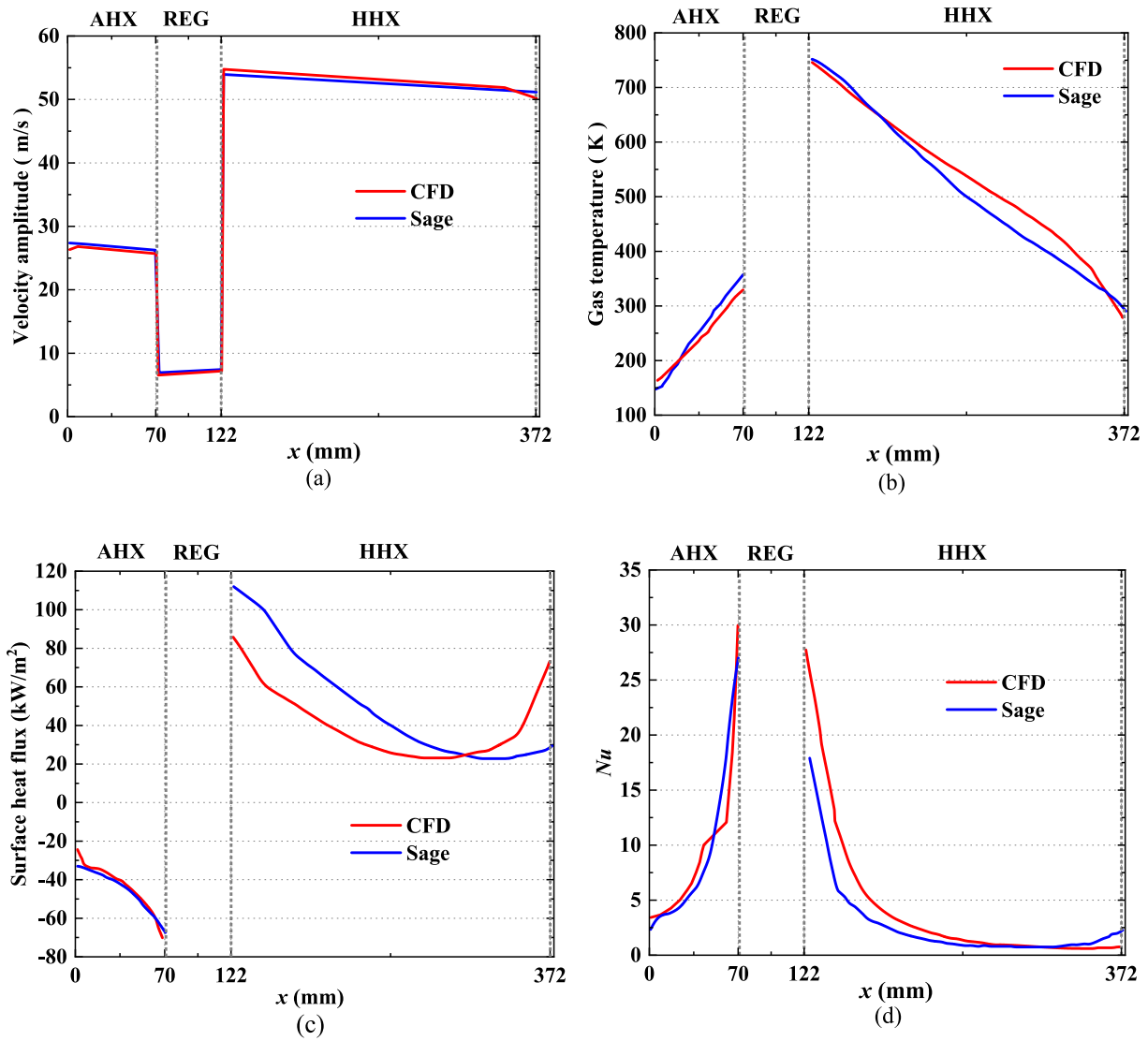


Fig. 3. Comparison of the Sage model and CFD model in terms of (a) velocity amplitude, (b) gas temperature, (c) time-average surface heat fluxes, and (d) time-average Nusselt number inside the ECU.

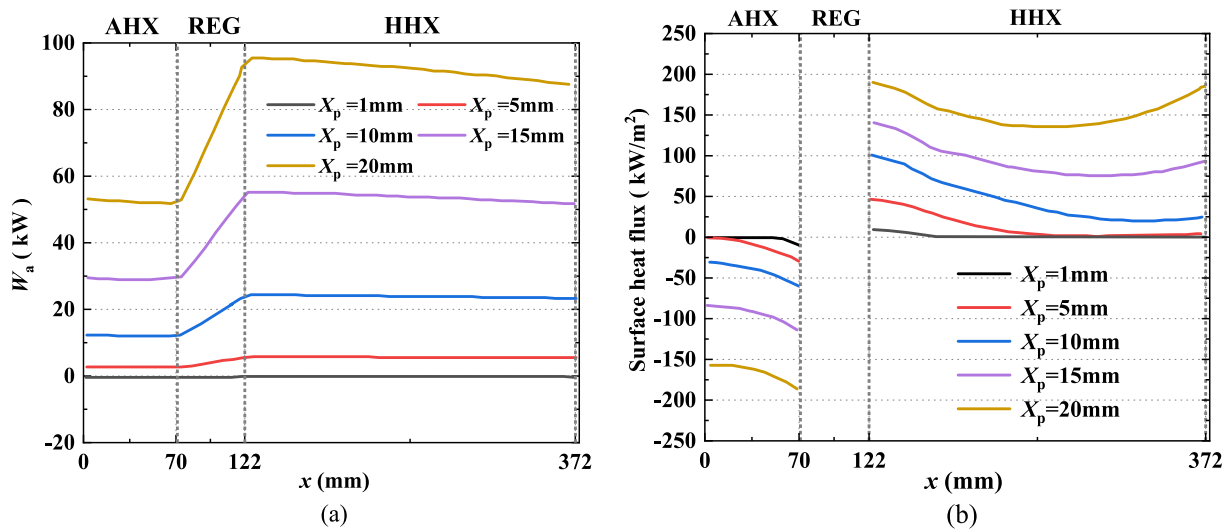


Fig. 4. Distributions of (a) time-average acoustic power, and (b) time-average surface heat fluxes inside the ECU at different displacement amplitudes. These results are obtained by the Sage model.

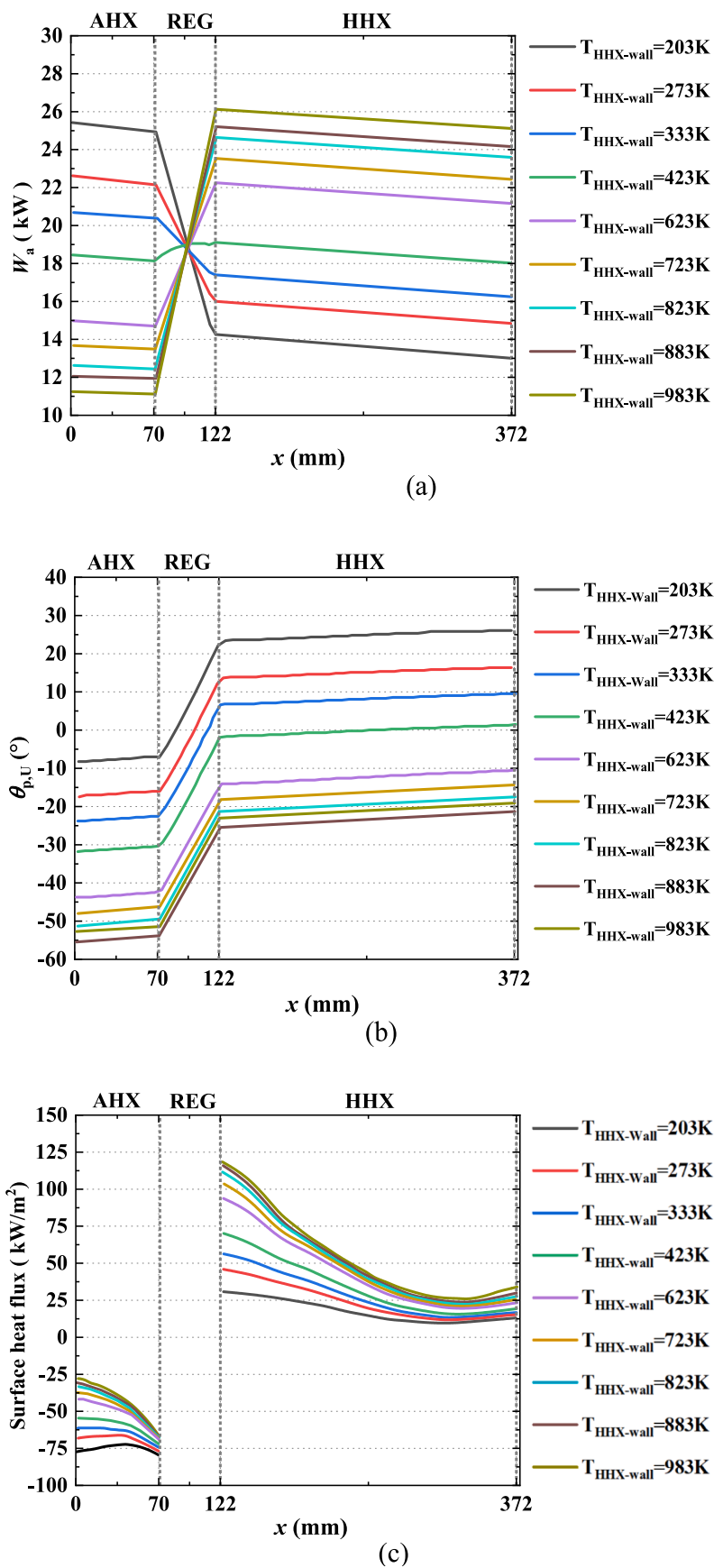


Fig. 5. Distributions of (a) time-average acoustic power, (b) phase difference between  $p$  and  $U$ , and (c) time-average surface heat fluxes inside the ECU at different HHX wall temperatures. These results are obtained by the Sage model.

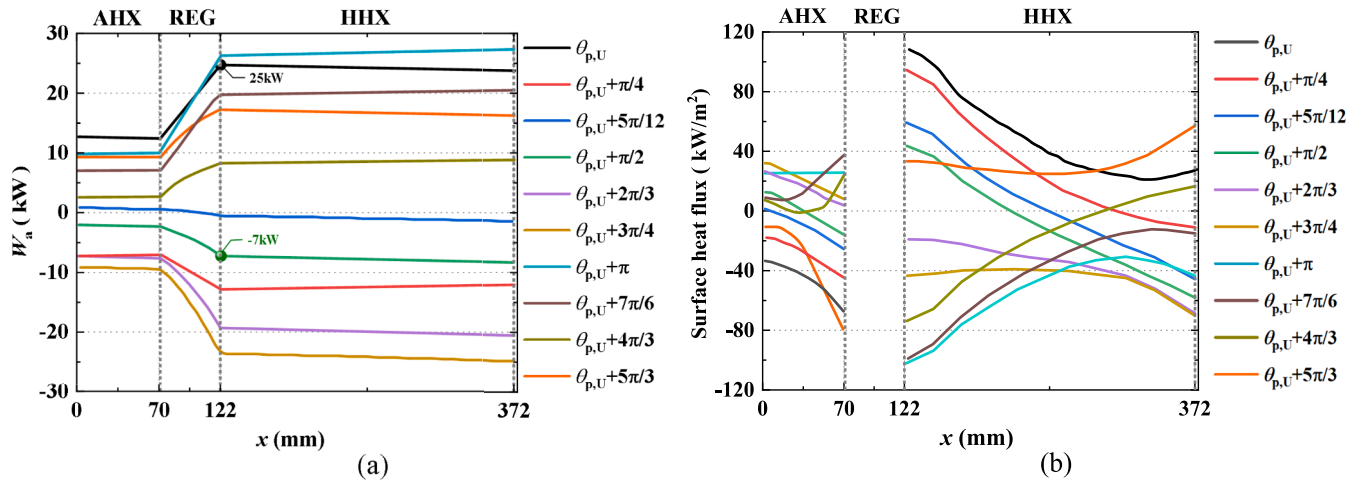


Fig. 6. Distributions of (a) time-average acoustic power and (b) time-average surface heat fluxes inside the ECU at different acoustic phase differences. These results are obtained by the Sage model.

Table 4  
Performance indexes of OFHXs at different thermal boundaries.

Thermal boundaries	Temperature boundary	Heat flux boundary	Convection boundary
$Q_{HHX}$ (W)	23,650	23,640	23,650
$Q_{AHX}$ (W)	12,700	12,540	12,600

heat exchanger [26], while also integrating numerical simulations to verify and interpret the experimental results [27].

It is important to choose suitable research methods when dealing with oscillating flow heat transfer problems of Stirling systems. As mentioned above, some available heat transfer models have been studied and compared with experimental findings, demonstrating the precision of the numerical simulations. Therefore, numerical simulation is the priority research method option for the design or optimization of Stirling systems. Different numerical methodologies have their pros and cons, and unfortunately, a comprehensive comparison between low-order numerical models and the CFD simulations on Stirling systems is lacking. What's more, the former studies on oscillating flow heat transfer mainly concentrated on low-power (generally lower than 5 kW) Stirling engine generators. As the power capacity of these generators rises, the heat transfer characteristics of the ECU will change accordingly. However, the heat transfer behaviours of ECUs under high power conditions are still unclear, and it is necessary to conduct a detailed and sensitive analysis of the heat transfer characteristics of these engine units.

To bridge these research gaps, in this study, the ECU of a 10 kW FPSG was simulated using both the Sage and CFD models. The computational results of the two models were compared and analysed for differences, with a detailed analysis of the heat exchanger's heat transfer characteristics under rated conditions. Utilizing the Sage model, a comprehensive analysis was conducted on the heat transfer characteristics of the ECU at a high-power level, this analysis proves advantageous in elucidating the flow heat transfer principles of the heat exchanger, thus guiding the design of a high-power FPSG.

In the subsequent Sections, Section 2 gives the configuration and structural parameters of the system under consideration. Section 3 presents the simulation models and their validation process, while Section 4 delves into the parameter sensitivity of the ECU. Lastly, Section 5 summarizes the main findings and conclusions derived from this research.

### System configuration

Fig. 1 presents a detailed schematic of the FPSG considered in this work. The generator is designed with an output power of 10 kW. In Fig. 1 (a), the FPSG integrates an FPSE and a dual-opposed LA. The ECU comprises several essential components, including a compression space which is connected to an annular AHX, and an expansion space which is connected to an annular HHX. Additionally, an annular REG is sandwiched between the AHX and the HHX, and is coaxial with both the AHX and the HHX. A displacer, which is deployed along the centre line of the annular HHX, is supported by planner springs mounted inside the bottom bounce space. Fig. 1(b) illustrates the cross-section view of the annual HHX along its radial direction. The HHX is coupled with 16 straight heat pipes, and the evaporation section of each heat pipe is integrated with the nuclear reactor core, and the condensation section is inserted into the heat pipe shell of the HHX, facilitating the transfer of heat produced by the reactor core to the working gas inside the HHX. To complete the heat transfer, the working gases traverse back and forth within the rectangular gas passages of the HHX. The dual-opposed LA is composed of two identical single-piston LA units and each unit includes a power piston, an electromagnetic conversion circuit, and a bounce space. Such a configuration could cancel out the vibrations between the two dual-opposed power pistons. The structural parameters of the FPSG are detailed in Table 1. Additionally, Table 2 provides the operating conditions of this system.

### Methodology

To perform a comprehensive comparison between low-order numerical models and the CFD simulations on a specific Stirling system, meanwhile reveal the heat transfer behaviours of ECUs under high power conditions, in this section, the ECU of a 10 kW FPSG was simulated using both the Sage and CFD models. The two different numerical models are introduced in this section.

#### Sage model

The Sage software is a commercial calculation platform developed by Gedeon [28], mainly for the general design calculation of thermoacoustic machines [29–32] and Stirling engines [33–36]. It encapsulates the gas flow, heat transfer, and other model details corresponding to actual physical components in specific model instances through a graphical interface. Users can establish simulation models for different Stirling/thermoacoustic machines by connecting these model instances

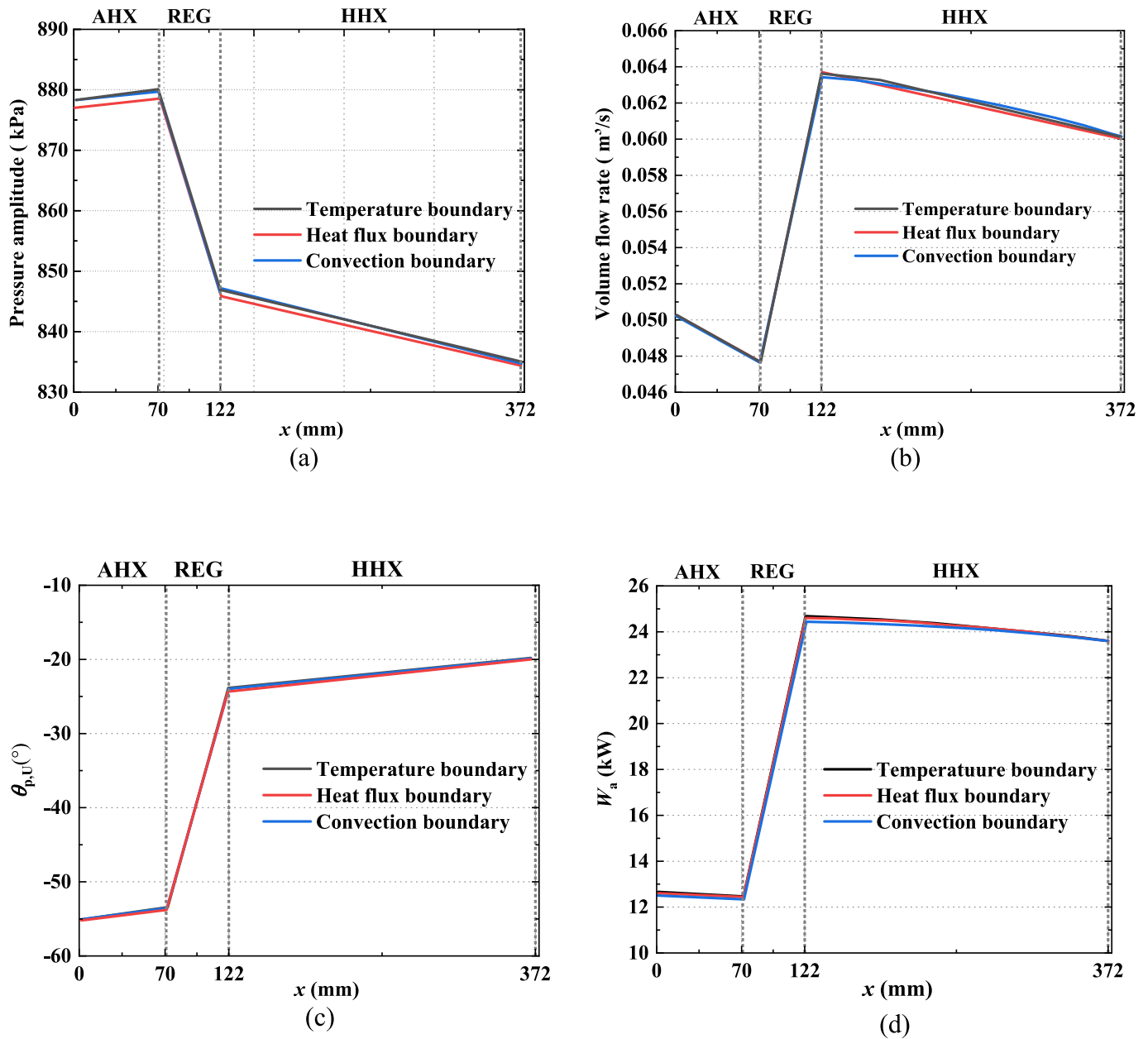


Fig. 7. Distributions of (a) pressure wave amplitude, (b) volume flow rate amplitude, (c) acoustic phase difference, and (d) time-average acoustic power at different thermal boundaries. These results are obtained by the Sage model.

according to the machines' configuration, and couple the parameters across these model instances with fundamental conservation equations, ultimately achieving the solution and multi-parameter collaborative optimization of the entire machine. Appendix A provides a detailed introduction to the governing equations and root interface of the Sage model as well as the experimental validation of the model.

#### CFD model

Computational fluid dynamics (CFD) is a high-order numerical method employed to analyse fluid flow and heat transfer characteristics, particularly in complex components such as OFHXs. To understand the intricate behaviour of fluids, it is essential to solve the fundamental governing equations of fluid mechanics, namely the continuity equation, the Navier-Stokes equations, and the energy equation. The process commences with defining the system's geometry and creating meshes that discretize this geometry into smaller computational units.

Subsequently, an appropriate physical model is selected based on the flow characteristics to simulate both transient and steady-state behaviours of the fluid under specified boundary conditions. The CFD model in this paper is based on ANSYS Fluent software. To reduce the amount of computational mesh (thus shortening the calculation time) while maintaining high calculation accuracy, the three-dimensional (3D) model is reasonably simplified into a two-dimensional (2D) model. For the CFD model, the simplification methodology, governing equations and boundary conditions are described in detail in Appendix B.

#### Results and discussions

##### Comparisons between the Sage and CFD results

Table 3 compares the calculation results of the Sage and 2D CFD models based on the geometric model in Appendix B Fig. B1(b) under the rated operating condition. As shown in the table, both calculations

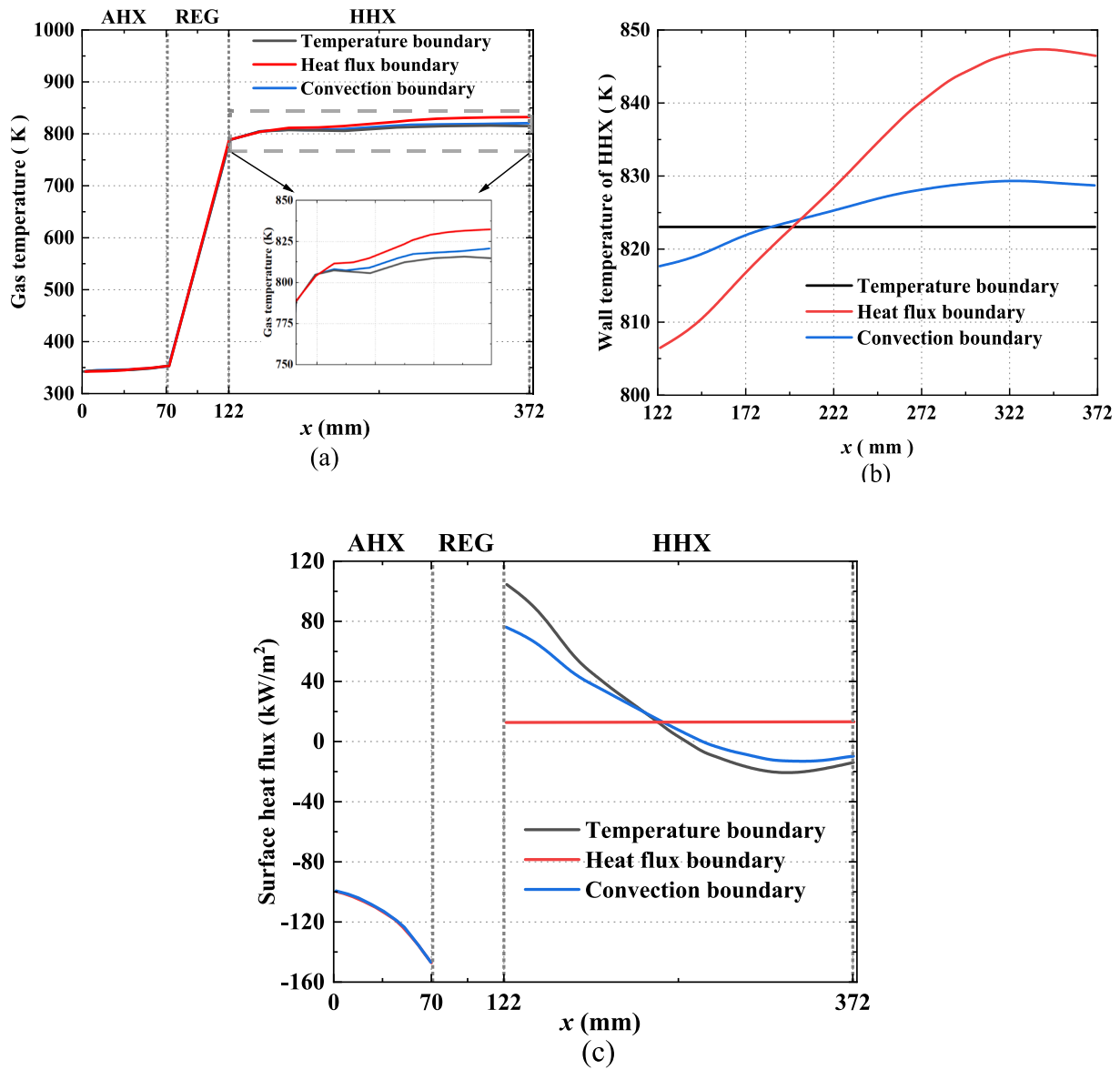


Fig. 8. Distributions of (a) gas temperature, (b) wall temperature of the HHX, and (c) time-average surface heat fluxes inside the ECU at different thermal boundaries. These results are obtained by the Sage model.

use the same piston boundaries, so the volume flow rates at the piston interface of the compression space and the expansion space are the same. The magnitudes of the time-averaged energy obtained by the two models are similar, with a difference of around 15 %, indicating that the Sage and CFD models are comparable.

Fig. 2 compares the pressure amplitude distribution in the ECU under the rated conditions obtained by the two different numerical methods. As illustrated in Fig. 2, the CFD model shows a higher pressure amplitude than the Sage model in both the AHX and REG sections. Conversely, for the HHX section, the CFD model shows a lower pressure amplitude relative to the Sage model. The maximum difference in the pressure amplitude between the two different numerical methods in the AHX is 40 kPa, while the maximum difference in the HHX reaches 60 kPa. This is because the one-dimensional Sage model is unable to directly capture localized losses caused by complex flow variations, and the existing heat exchanger model instances in Sage cannot automatically adjust the localized resistances based on the relative structural features between the components; therefore, it needs to set up the associated losses manually. On the contrary, the 2D CFD simulation can capture the variations in flow field characteristics, including the jets in the AHX's

and the HHX's channels, which results in the presence of sudden pressure changes at the contact surfaces of adjacent components.

Fig. 3(a)-(d) shows a comparison of the distributions of velocity amplitude, gas temperature, time-averaged surface heat fluxes, and time-averaged Nusselt number obtained by the CFD and Sage models in the ECU under rated operating conditions. Fig. 3(a)-(b) displays the calculation results of the two models that are very close to each other in terms of the velocity and the gas temperature. The variations of the velocity amplitude and the gas temperature obtained by the two different numerical methods are almost the same for the AHX. Therefore, the surface heat fluxes obtained by the two different numerical methods are close to overlap in Fig. 3(c). However, a small difference between the results obtained by the two models for the surface heat fluxes in the HHX. Based on Eq. (A9), it is known that the influence of the time-averaged surface heat flux of the heat exchanger is mainly concentrated on the Nusselt number. Fig. 3(d) shows the time-averaged Nusselt number  $Nu$ , of the AHX and HHX, calculated by the CFD model and the Sage model respectively based on Eqs (A10)-(A11). The distribution of  $Nu$  along the AHX and HHX is consistent in both models, with larger values near the REG side. This further indicates that the heat



exchangers in the Sage and CFD models have similar heat transfer characteristics. According to Eq. (A10),  $Nu$  in the Sage model is a function of the resistance coefficient and Reynolds number  $Re$  along the heat exchanger. Therefore, the value of  $Nu$  inside the AHX and HHX is determined by the fluid velocity and the friction.

According to the analysis mentioned above, the local resistance in an OFHX due to structural variations (between the heat exchanger and adjacent components) and the non-linear phenomena during operation minimally impact the internal heat transfer of the system. The friction within the heat exchanger can be determined using the Sage model. Despite being founded on one-dimensional governing equations, the Sage model provides calculations that are fairly close to those of the CFD model, with some differences in quantity. Therefore, we can use Sage model for engineering design of OFHXs and assess their heat transfer characteristics.

#### Heat transfer characteristics sensitivity analysis

Given the significantly faster calculation speed of the Sage model in comparison to the CFD model, this section analysis the sensitivity of the heat transfer characteristics of the ECU to different piston displacement amplitudes, HHX wall temperatures, acoustic phase differences, and thermal boundary conditions using the Sage model.

##### Effect of piston displacement amplitude

Fig. 4 (a)-(b) displays the distributions of time-average acoustic power and time-average surface heat fluxes inside the ECU at different piston displacement amplitudes, respectively. With the increase of displacement of the compression and expansion pistons, the gas velocity inside both the AHX and the HHX increases, the time-average acoustic power of the ECU goes up, and the capability for acoustic power amplification of the REG strengthens, enhancing the thermoacoustic effect inside the REG. The time-average surface heat fluxes of the AHX and the HHX have obvious inlet and outlet effects. At low velocities, the inlet and outlet effects of the HHX and AHX have symmetry and are concentrated on the REG side. With the velocity increases, the inlet and outlet effects become asymmetric, and the time-average wall surface heat flux of the HHX extends to the other side, causing uneven internal heat transfer. These results indicate that the effective length of the OFHX should match the displacement amplitude of its piston.

##### Effect of HHX wall temperature

Fig. 5(a)-(c) displays the distributions of time-average acoustic power, acoustic phase, and time-average surface heat fluxes inside the ECU at different HHX wall temperatures of the ECU, respectively. In calculations, we fixed the AHX wall temperature at 333 K and increased the HHX wall temperature from 203 K to 983 K. When the HHX wall temperature gradually increases, the temperature difference between the engine's hot end and the cold end goes up, the thermoacoustic effect is enhanced, and the acoustic power inside the ECU increases. Meanwhile, the AHX and the HHX heat transfer capacity are proportional to the temperature difference between the cold and hot ends. Increasing the HHX wall temperature, the AHX, and the HHX heat transfer would be enhanced. However, when the HHX wall temperature exceeds 823 K, the trend of the acoustic field change in the ECU is weakened, the thermoacoustic effect tends to be saturated, and the heat transfer characteristics of the AHX and the HHX are no longer significantly changed. It is shown that for the ECU studied in this paper, the optimal HHX wall temperature is around 823 K.

##### Effect of acoustic phase difference

Unlike steady-state flow exchangers, in OFHXs, the enthalpy flow is affected by the interaction between the flow and temperature fields. When the acoustic phase difference between mass flow rate and temperature changes, the flow and temperature fields of the gas inside the OFHX will be changed accordingly. Therefore, exploring how the

acoustic phase difference influences the heat transfer characteristics of the OFHX is crucial. In this paper, the variation in acoustic phase difference (phase difference between  $p$  and  $U$ ) was achieved by keeping the displacement amplitudes of compression and expansion pistons at the rated condition and adjusting the velocity phase difference between the two pistons from 0 to  $2\pi$ .

In Fig. 6(a)-(b), the time-averaged acoustic power and time-averaged surface heat fluxes inside the heat exchangers change significantly with the acoustic phase difference. When the acoustic phase difference is increased by  $90^\circ$ , the mean acoustic power of HHX changes from 25 kW to  $-7$  kW, at which point the REG transitions from amplifying acoustic power to beginning to consume it. When the acoustic phase difference increases by  $135^\circ$ , the distributions of surface heat fluxes of the HHX and the AHX are gradually homogenized, and the heat transfer capacity is gradually reduced. When the acoustic phase difference increases by  $180^\circ$ , the inlet and outlet effects of the HHX surface heat flux are reversed in comparison with that observed at the initial acoustic phase difference. Specifically, the inlet and outlet effects are transformed from the surface heat flux at the original REG side higher than the expansion space side to that surface heat flux at the expansion space side higher than the REG side. The main cause for this phenomenon is the change in acoustic phase difference, which induces changes in both mass flow phase and temperature phase within HHX and AHX. The analysis above suggests that the primary factor impacting heat transfer in the OFHX is the acoustic phase difference.

##### Effect of thermal boundary

As mentioned before, examining the impacts of varying thermal boundaries on heat transfer in oscillating flow is crucial. The performance metrics of the two heat exchangers in the ECU are displayed in Table 4 for different thermal boundaries. The investigation in Table 4 reveals the influence of different thermal boundaries on heat transfer in oscillating flow under the same operating conditions. It should be noted that a unified temperature boundary was applied to the AHX and different thermal boundaries were applied to the HHX.

Fig. 7(a)-(d) illustrates the state parameter distributions within the ECU for different thermal boundaries. These include the amplitude of the pressure wave, the amplitude of the volume flow rate, the acoustic phase difference, and the acoustic power. The ECU continually operates under its rated conditions, maintaining constant piston velocity, unchanged pressure amplitude, and volume flow rate amplitude, resulting in consistent acoustic power, as depicted in Fig. 7(d). It can be inferred that with other parameters held constant, the acoustic power and acoustic field of the ECU are not affected by changes in thermal boundaries.

As depicted in Fig. 8(a)-(b), significant variations differences in the gas mean temperature and wall surface temperature of the HHX under different thermal boundaries. The HHX wall experiences a maximal temperature difference of 25 K, while the gas mean temperature exhibits a difference of 20 K. As highlighted in Fig. 8(c), despite discrepancies in temperature distributions, the heat transfer characteristics along the HHX wall remain consistent, exhibiting just a  $30 \text{ kW/m}^2$  difference near the REG side. This suggests that the heat transfer characteristics of the ECU are not excessively sensitive to the thermal boundaries, remaining within an acceptable range.

## Conclusions

To fill the research gaps of oscillating flow heat transfer of Stirling/thermoacoustic systems, in this work, we considered a 10 kW FPSG that integrates heat pipes. We performed a comparison of the numerical results derived from both the Sage model and the CFD model for the ECU. Furthermore, a detailed analysis was carried out on the heat transfer characteristics of the ECU under various operating conditions using the Sage model. From this research, we can conclude that:

- (1) Comparison of the Sage simulation results with the CFD simulation results at rated conditions shows that a discrepancy of approximately  $20 \text{ kW/m}^2$  in the surface heat flux calculations for the HHX. This difference arises from variations in model accuracy between the 1D Sage model and the 2D CFD model. However, both numerical methods yield consistent trends in the heat transfer distribution on the HHX wall. This indicates that the Sage model can reasonably describe the heat transfer distribution in an OFHX and can be used to predict the heat transfer characteristics of the ECU of an FPSE, which improves the efficiency of the design and optimization of free-piston Stirling machines.
- (2) Increasing the HHX wall temperature of the ECU, the thermoacoustic effect of the REG is enhanced, and the heat transfer of the AHX and the HHX is improved. When the wall temperature of the HHX exceeds 823 K, the thermoacoustic effect tends to be saturated, and at this time, a further increase of the HHX wall temperature will not significantly improve the heat transfer capacity of the AHX and HHX.
- (3) A change of  $90^\circ$  in the acoustic phase difference can directly lead to a 32 kW change in the acoustic power of the HHX, and the REG is directly transformed from amplifying acoustic power to consuming acoustic power. When the change of the acoustic phase difference is more than  $180^\circ$ , the inlet and outlet effects of the HHX are reversed in comparison with that of the initial acoustic phase difference. These results indicate that the heat transfer characteristics of the OFHX have significant operation-related characteristics. Therefore, quantitative, and qualitative study of the heat transfer characteristics of the OFHX is required based on specific acoustic field parameters.
- (4) Although different thermal boundaries lead to different wall and gas temperatures in the HHX under the same operating conditions, the maximum difference in wall heat flux is only  $30 \text{ kW/m}^2$ , while the ECU acoustic power remains unchanged in different thermal boundaries. This indicates that the change of thermal boundaries only affects the temperature field of the ECU.

The analysis in this paper not only combines the ECU to improve the applicability of the calculation results but also further analyzes the impact of various factors on the heat transfer characteristics of the ECU to identify the most sensitive factors, which can be used to guide the design and optimization of the ECU of a high-power FPSE, which will pave the way to achieve efficient integration with micro nuclear reactor in the future.

#### CRediT authorship contribution statement

**Haitao Wang:** Writing – original draft, Software, Methodology, Funding acquisition, Formal analysis, Data curation. **Yanyan Chen:** Writing – review & editing, Supervision, Software, Resources, Project administration, Methodology, Funding acquisition, Formal analysis. **Shunmin Zhu:** Writing – review & editing, Software, Resources, Methodology. **Limin Zhang:** Writing – review & editing, Validation, Supervision, Software, Methodology. **Guoyao Yu:** Writing – review & editing, Software, Resources, Project administration, Methodology, Conceptualization. **Huifang Kang:** Writing – review & editing. **Ercang Luo:** Writing – review & editing, Visualization, Validation, Supervision, Software, Resources, Project administration, Methodology, Funding acquisition.

#### Declaration of competing interest

The authors declare that they have no known competing financial interests or personal relationships that could have appeared to influence the work reported in this paper.

#### Acknowledgments

This research received financial support from the National Key R&D Program (No.2021YFC28026003) and the National Natural Science Foundation of China (No. 51876214 and No. 52306031).

#### Appendix A. Supplementary data

Supplementary data to this article can be found online at <https://doi.org/10.1016/j.seta.2025.104243>.

#### Data availability

Data will be made available on request.

#### References

- [1] Mazzetti A, Gianotti Pret M, Pinarello G, Celotti L, Piskacev M, Cowley A. Heat to electricity conversion systems for moon exploration scenarios: a review of space and ground technologies. *Acta Astronaut* 2019;156:162–86. <https://doi.org/10.1016/j.actaastro.2018.09.025>.
- [2] Zhu S, Yu G, Jiang C, Wang T, Zhang L, Wu Z, et al. A novel thermoacoustically-driven liquid metal magnetohydrodynamic generator for future space power applications. *Energy Convers Manag* 2022;258:115503. <https://doi.org/10.1016/j.enconman.2022.115503>.
- [3] El-Genk MS. Space nuclear reactor power system concepts with static and dynamic energy conversion. *Energy Convers Manag* 2008;49:402–11. <https://doi.org/10.1016/j.enconman.2007.10.014>.
- [4] McClure PR, Poston DI, Gibson MA, Mason LS, Robinson RC. Kilopower project: the KRUSTY fission power experiment and potential missions. *Nucl Technol* 2020;206: 2. <https://doi.org/10.1080/00295450.2020.1722554>.
- [5] Orłowska A. Development of the European Radioisotope Stirling Generator (ERSG). *Int. Cryocoolers Conf.* 20, 2018.
- [6] Hoshino T. Preliminary Test Results on 200 We Free-Piston Stirling Engine Converter. 1st Int. Energy Convers. Eng. Conf. IECEC, Portsmouth, Virginia: American Institute of Aeronautics and Astronautics; 2003. doi: 10.2514/6.2003-6094.
- [7] Wang H, Chen Y, Luo J, Zhang L, Kang H, Luo E, et al. A novel high-power free-piston Stirling engine generator with integrated heat pipes for thermal-to-electric conversion of clean energy. *Energy* 2025;314:134218. <https://doi.org/10.1016/j.energy.2024.134218>.
- [8] Jun Park K, Soo Kim E, Beom JY. Development of dynamic simulation model for 20 kWe micro heat pipe fission battery with dual power conversion system. *Appl Therm Eng* 2024;124505. <https://doi.org/10.1016/j.applthermaleng.2024.124505>.
- [9] Zhu S, Yu G, Liang K, Dai W, Luo E. A review of Stirling-engine-based combined heat and power technology. *Appl Energy* 2021;294:116965. <https://doi.org/10.1016/j.apenergy.2021.116965>.
- [10] Vahidi Bidhendi M, Abbasi Y. Exploring dynamic operation of a solar dish-stirling engine: validation and implementation of a novel TRNSYS type. *Sustain Energy Technol Assess* 2020;40:100765. <https://doi.org/10.1016/j.seta.2020.100765>.
- [11] Piccolo A. Design issues and performance analysis of a two-stage standing wave thermoacoustic electricity generator n.d.
- [12] Huntingford F, Kisha W. Algorithmic optimisation of the electrical power output of a low-cost, multicore thermoacoustic engine with varying resonator pressure. *Sustain Energy Technol Assess* 2022;49:101776. <https://doi.org/10.1016/j.seta.2021.101776>.
- [13] Pamuk M. A new heat transfer correlation for oscillating fluid flow. *Therm Sci* 2018;22:2459–66. <https://doi.org/10.2298/TSCI160126215P>.
- [14] Peacock JA, Stairmand JW. Film gauge calibration in oscillatory pipe flow. *J Phys [E]* 1983;16:571–6. <https://doi.org/10.1088/0022-3735/16/6/026>.
- [15] Xin F. Flow and heat transfer performance of reciprocating oscillatory flow in a Stirling engine compared to steady unidirectional flow. *Int J Therm Sci* 2024.
- [16] Richardson EG, Tyler E. The transverse velocity gradient near the mouths of pipes in which an alternating or continuous flow of air is established. *Proc Phys Soc* 1929;42:1–15. <https://doi.org/10.1088/0959-5309/42/1/302>.
- [17] Gedeon D. Mean-parameter modeling of oscillating flow. *J Heat Transf* 1986;108: 513–8. <https://doi.org/10.1115/1.3246964>.
- [18] Nika P, Bailly Y, Guermeur F. Thermoacoustics and related oscillatory heat and fluid flows in micro heat exchangers. *Int J Heat Mass Transf* 2005;48:3773–92. <https://doi.org/10.1016/j.ijheatmasstransfer.2005.02.006>.
- [19] Liu J, Garrett SL. Relationship between Nusselt number and the thermoviscous (Rott) functions. *J Acoust Soc Am* 2006;119:1457–62. <https://doi.org/10.1121/1.2165000>.
- [20] Clark JP, Ward WC, Swift GW. Design environment for low-amplitude thermoacoustic energy conversion (DeltaEC). *J Acoust Soc Am* 2007;122.
- [21] Li Z, Haramura Y, Tang D, Guo C. Analysis on the heat transfer characteristics of a micro-channel type porous-sheets Stirling regenerator. *Int J Therm Sci* 2015;94: 37–49. <https://doi.org/10.1016/j.ijthermalsci.2015.02.011>.

- [22] Costa SC, Barrutia H, Esnaola JA, Tutar M. Numerical study of the heat transfer in wound woven wire matrix of a Stirling regenerator. *Energy Convers Manag* 2014; 79:255–64. <https://doi.org/10.1016/j.enconman.2013.11.055>.
- [23] Di Meglio A, Massarotti N. CFD modeling of thermoacoustic energy conversion: a review. *Energies* 2022;15:3806. <https://doi.org/10.3390/en15103806>.
- [24] Bitsikas P, Rogdakis E, Dogkas G. CFD study of heat transfer in Stirling engine regenerator. *Therm Sci Eng Prog* 2020;17:100492. <https://doi.org/10.1016/j.tsep.2020.100492>.
- [25] El-Ghafour SA, El-Ghandour M, Mikhael NN. Three-dimensional computational fluid dynamics simulation of stirling engine. *Energy Convers Manag* 2019;180: 533–49. <https://doi.org/10.1016/j.enconman.2018.10.103>.
- [26] Nsofor EC, Celik S, Wang X. Experimental study on the heat transfer at the heat exchanger of the thermoacoustic refrigerating system. *Appl Therm Eng* 2007;27: 2435–42. <https://doi.org/10.1016/j.applthermaleng.2007.03.008>.
- [27] Piccolo S, Guglielmino. Convection heat transfer coefficients in thermoacoustic heat exchangers: an experimental investigation. *Energies* 2019;27:4525. <https://doi.org/10.3390/en12234525>.
- [28] Gedeon D. Sage - Object-oriented software for Stirling machine design. Intersoc. Energy Convers. Eng. Conf., Monterey,CA,U.S.A.: American Institute of Aeronautics and Astronautics; 1994. doi: 10.2514/6.1994-4106.
- [29] Xu J, Hu J, Luo E, Zhang L, Dai W. A cascade-looped thermoacoustic driven cryocooler with different-diameter resonance tubes. Part I: theoretical analysis of thermodynamic performance and characteristics. *Energy* 2019;181:943–53. <https://doi.org/10.1016/j.energy.2019.06.009>.
- [30] Chi J, Yang Y, Wu Z, Yang R, Li P, Xu J, et al. Numerical and experimental investigation on a novel heat-driven thermoacoustic refrigerator for room-temperature cooling. *Appl Therm Eng* 2023;218:119330. <https://doi.org/10.1016/j.applthermaleng.2022.119330>.
- [31] Pang X, Wang X, Dai W, Li H, Wu Y, Luo E. Theoretical and experimental study of a gas-coupled two-stage pulse tube cooler with stepped warm displacer as the phase shifter. *Cryogenics* 2018;92:36–40. <https://doi.org/10.1016/j.cryogenics.2018.03.008>.
- [32] Wang X, Wu Z, Zhang L, Hu J, Luo E. Traveling-wave thermoacoustic refrigerator for room temperature application. *Int J Refrig* 2020;120:90–6. <https://doi.org/10.1016/j.ijrefrig.2020.08.021>.
- [33] Chang D, Hu J, Sun Y, Zhang L, Chen Y, Luo E. Numerical investigation on key parameters of a double-acting free piston Stirling generator. *Energy* 2023;278: 128003. <https://doi.org/10.1016/j.energy.2023.128003>.
- [34] Zhu S, Yu G, Li X, Dai W, Luo E. Parametric study of a free-piston Stirling cryocooler capable of providing 350 W cooling power at 80 K. *Appl Therm Eng* 2020;174:115101. <https://doi.org/10.1016/j.applthermaleng.2020.115101>.
- [35] Jia Z, Wang R, Hu J, Zhang L, Wu Z, Chen Y, et al. Study on the coupling between engine and alternator in a free-piston Stirling generator. *Appl Therm Eng* 2022; 217:119222. <https://doi.org/10.1016/j.applthermaleng.2022.119222>.
- [36] Park J, Ko J, Kim H, Hong Y, Yeom H, Park S, et al. The design and testing of a kW-class free-piston Stirling engine for micro-combined heat and power applications. *Appl Therm Eng* 2020;164:114504. <https://doi.org/10.1016/j.applthermaleng.2019.114504>.